Resonating Power Decoupling Using Multifunctional Bidirectional DC/DC Converter in Hybrid Railway Traction Application

Lailai Shen, Jie Chen, *Member, IEEE*, Zheming Jin, *Member, IEEE*, Zhigang Liu,
Dao Zhou, *Senior Member, IEEE*, and Chao Wu, *Member, IEEE*

***Abstract*—For the single-phase high-power railway traction system, the inevitable second-order resonating power has become a critical issue to the traction system. In this article, a power-decoupling solution is proposed to replace the conventional passive *LC* resonance filter by utilizing the buck-type bidirectional dc/dc converter (BBDC) of hybrid electric multiple units, which is designed to power the train in nonelectrified routes using the on-board battery. By considering both the current ripples in the battery mode and the power decoupling in the catenary mode, the corresponding parameter design process of the BBDC is presented. Based on the power coupling phenomenon and the spectrum characteristic of the BBDC, a direct resonance control method is proposed to decouple the low-order resonating power. Simulations and experiments are carried out to validate the effectiveness of the new proposal. The results demonstrate that the proposal is almost the same as using the conventional passive *LC* resonance filter for power decoupling in both steady and dynamic operation scenarios.**

***Index Terms*—Buck-type bidirectional dc/dc converter (BBDC), power decoupling, railway traction, resonating power, single-phase application.**

I. INTRODUCTION

THE electrified railway is demanded in many countries to the merits of its safety, high speed, punctuality, mass transport capacity, and energy efficiency. Currently, in most countries, the electrified routes are powered by overhead contact lines (i.e., the catenary), which is a typical single-phase ac power network. Meanwhile, the two-stage (i.e., ac–dc–ac) power electronic-based traction system has become the state-of-the-art solution for both locomotive and electric multiple units (EMUs), which are typically high-speed bullet trains. However, for these systems, the instantaneous input power fed by the catenary will naturally contain a resonating component at twice the grid frequency (i.e., second order), resulting in the fluctuating dc-link voltage at the same frequency [1]–[3]. One step further, with such fluctuating dc-link voltage, the traction inverter will be affected, and the traction motors will suffer from undesired current harmonics, torque pulsation, additional power loss, overheating, etc. [4], [5]. These will lead to accelerated aging of the motor and irregular wheel wearing.

Currently, as the state-of-the-art solution in railway traction applications, a dedicated passive *LC* resonance filter tuned at twice the grid frequency is connected in parallel with the dc-link capacitor to filter out the second-order fluctuating voltage ripples (i.e., the PLC method) [6]. However, this hardware solution occupies a large volume and heavyweight. Moreover, the capacitor also inevitably suffers from its aging issue, which will worsen the performance over time [7], [8]. Hence, a software-based solution of suppressing the second-order voltage fluctuation is valuable for practical applications.

For low-power customer electronics and electric vehicle applications [9]–[13], it is common to use an auxiliary circuit to decouple the second-order resonating power. However, for the conventional EMUs, the decoupling circuit is hardly reported because it is not cost-efficient compared with the dedicated passive *LC* resonance filter. In our previous work, a new type of hybrid EMU (HEMU) is proposed and developed to allow seamless operation on both electrified and nonelectrified routes [14]. The traction system of HEMU integrates an additional buck-type bidirectional dc/dc converter (BBDC) to power the train by the large-scale on-board battery for nonelectrified routes and emergency situations [14], [15]. In this sense, the train's flexibility, reliability, and functionality are greatly improved. However, a potential problem of the HEMU is that the BBDC has not been fully utilized as it is often in standby mode when the catenary is available. It is noteworthy that the BBDC also contains a nondedicated *LC* branch, making it capable of decoupling the resonating power. For this reason, this article proposes utilizing the BBDC (i.e., the UBBDC method) for power decoupling in catenary mode to make the HEMU more compact, more adaptable, and more cost-efficient.

Manuscript received February 3, 2021; revised May 13, 2021; accepted July 16, 2021. Date of publication July 29, 2021; date of current version September 16, 2021. This work was supported by the Fundamental Research Funds for the Central Universities under Grant 2019YJS175. Recommended for publication by Associate Editor X. Ruan. *(Corresponding authors: Jie Chen; Zheming Jin.)*

Lailai Shen, Jie Chen, and Zheming Jin are with the School of Electrical Engineering, Beijing Jiaotong University, Beijing 100044, China (e-mail: 18117017@bjtu.edu.cn; jiechen@bjtu.edu.cn; zhmjin@bjtu.edu.cn).

Zhigang Liu is with the School of Electrical Engineering, Beijing Jiaotong University, Beijing 100044, China, and also with the Beijing Electrical Engineering Technology Research Center, Beijing Jiaotong University, Beijing 100044, China (e-mail: zhgliu@bjtu.edu.cn).

Dao Zhou and Chao Wu are with the Department of Energy Technology, Aalborg University, 9100 Aalborg, Denmark (e-mail: zda@et.aau.dk; cwu@et.aau.dk).

Color versions of one or more figures in this article are available at https://doi.org/10.1109/TPEL.2021.3100703.

Digital Object Identifier 10.1109/TPEL.2021.3100703

In the existing literature [16]–[19], the design process of the decoupling capacitor for low-power applications has been fully studied. However, in high-power applications, the design principle shall be different. The low switching frequency requires a significantly larger filter inductor (typically more than 1 mH). For this reason, neither the energy stored by the inductor nor the voltage drop over the inductor is neglectable. Consequently, the conventional design principles in [16]–[19] are no longer feasible.

As for the control strategy, the power-decoupling control based on the BBDC can be performed by either the direct-power-decoupling method or the automatic-power-decoupling method [20]. Almost all the direct-power-decoupling methods are calculating the resonating power in an open-loop manner [11], [17], [21]–[26]. The open-loop manner is easy to implement; however, it is sensitive to the variations of parameters and disturbances. In [27], a closed-loop direct-power-decoupling method is proposed to solve the problem. Nevertheless, the resonating power calculation process and the control system are complexed, and the precision of such a method is still challenging. Differing from the direct-power-decoupling method, automatic-power-decoupling methods are used to design a closed-loop control system for the dc-link voltage; thereby, the low-order voltage ripples can be eliminated directly. As the calculation of the resonating power is not needed anymore, the control structure can be simpler, and the performance is more robust [28]–[31]. In [28] and [29], the nonlinear controller is proposed to obtain a fast dynamic performance, and the control bandwidth needs to be sufficiently high to facilitate the controller design. Unfortunately, it is impractical to have such a high control bandwidth in high-power applications due to low switching frequency and long control delay [30], [31]. In [32], a proportional–integral (PI) controller and a bandpass filter are used to mitigate the dc-link voltage ripple at twice the grid frequency. However, higher order voltage ripples can be introduced. Although the multiproportional–resonant controller is used to suppress the higher order voltage ripples in [33], the high control bandwidth is still required. Besides, the resonance peak of the nondedicated *LC* branch in the BBDC may lead to instability. Therefore, the control methods used for power decoupling in the low-power applications are not fully applicable to the case study, and it is necessary to reformulate a proper control method in this case.

In this article, a power-decoupling solution is proposed by utilizing the standby BBDC for the HEMU traction system. Thus, the conventional passive *LC* filter can be removed. By considering the filter inductor's impact, the power-decoupling capability of the BBDC is analyzed in detail, and the power coupling phenomenon, which is significant in the high-power nondedicated power-decoupling circuit, is revealed. By considering the influence of the filter inductor and the power coupling feature, a new parameter design process of the BBDC is presented based on the operating condition of the entire traction system. Based on the resonating power spectrum shifting feature of the BBDC, a direct resonance control method is proposed to regulate the low-order resonating power into the nondedicated *LC* branch. Therefore, the dc-link voltage fluctuation can be buffered. To verify the new proposal, simulations and experiments are carried out. The results demonstrate that the performance with the proposal is almost the same as that with the PLC method in both steady and transient states.

TABLE I
KEY PARAMETERS OF THE HEMU TRACTION DRIVE SYSTEM

Parameter	Value
4QC rated power	2×460 kW
Switching frequency of the BBDC	1 kHz
AC rated voltage V_g	1273 V
Grid filter L_g	2.08 mH
Inductor in passive filter L_r	0.36 mH
Capacitor in passive filter C_r	7 mF
DC-link capacitor C_d	4×2 mF
DC-link rated voltage U_d	1650 V
Battery rated voltage U_{bat}	1100 V

The main contributions of this article can be summarized as follows.

1) The power coupling feature is revealed, and a power-decoupling solution is proposed for the HEMU to replace the conventional passive *LC* resonance filter.
2) A new parameter design process is presented for a high-power power-decoupling circuit, which considers the influence of a large inductor and the power coupling feature.
3) Based on the resonating power spectrum shifting feature, a direct resonance control method is proposed, which is designed to regulate the low-order resonating power with nondedicated *LC* circuit.

The rest of this article is organized as follows. In Section II, the source of the resonating power is analyzed, and the power coupling feature of the BBDC is unveiled in detail. In Section III, the parameters for the BBDC are designed, and the direct resonance control method is proposed to regulate the resonating power. In Section IV, the simulations and experimental results verify the proposed method. Finally, Section V concludes this article.

II. RESONATING POWER AND POWER COUPLING FEATURE

A. Resonating Power Analysis

The main topology and the key parameters of the HEMU traction drive system are shown in Fig. 1 and Table I, respectively. The front-end single-phase voltage-source four-quadrant converter (4QC) is fed by the catenary to power the whole traction drive system. The BBDC, which is composed of the Insulated Gate Bipolar Transistor (IGBT) module, the filter inductor L_{cs}, the filter capacitor C_{cs} (called the decoupling capacitor for resonating power), and the breaker $K1$, is used for charging and discharging the on-board battery. Besides, double 4QCs and double BBDCs are connected in parallel to increase the system power level. The dc-link voltage u_d is supported and filtered by the dc-link capacitor C_d, and the motors are driven by a three-phase voltage-source inverter. When the ac power is available, the traction drive system of the HEMU is fed by the

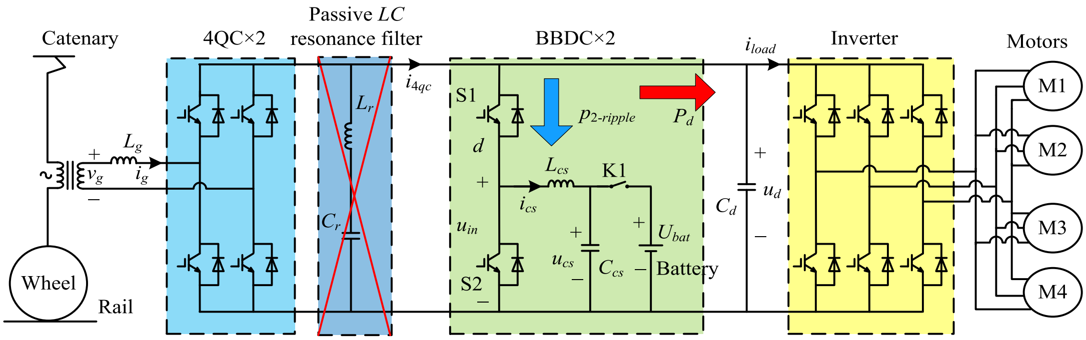

Fig. 1. Main topology of the HEMU traction drive system.

catenary. As both the input voltage and current of the 4QC have sinusoidal shapes, the instantaneous input power to the traction drive system can be expressed as follows:

$$\begin{aligned} p_{\text{in}} &= I_g \sin(\omega t - \varphi) \left[V_g \sin(\omega t) - L_g \frac{d I_g \sin(\omega t - \varphi)}{dt} \right] \\ &= \frac{V_g I_g}{2} [\cos \varphi - \cos(2\omega t - \varphi)] - \frac{\omega L_g I_g^2}{2} \sin(2\omega t - 2\varphi) \end{aligned} \tag{1}$$

where V_g and I_g are the amplitudes of the input voltage and current, resepctively, ω is the grid angular frequency (100π rad/s), φ is the angle between the grid voltage and current, and L_g is the ac inductance. p_{in} consists of the dc power P_d supplied to the loads and the undesired second-order resonating power $p_{2\text{-ripple}}$, and they are expressed as

$$P_d = \frac{V_g I_g}{2} \cos \varphi \tag{2}$$

$$p_{2-\text{ripple}} = P_{2-\text{peak}} \sin(2\omega t + \theta) \tag{3}$$

where

$$P_{2-\text{peak}} = \sqrt{\left(\frac{V_g I_g}{2} \cos \varphi \right)^2 + \left(\frac{\omega L_g I_g^2 - V_g I_g \sin \varphi}{2} \right)^2}$$

$$\theta = -2\varphi + \tan^{-1} \left(\frac{V_g I_g \cos \varphi}{\omega L_g I_g^2 - V_g I_g \sin \varphi} \right).$$

With the conventional configuration, the dedicated passive *LC* resonance filter (L_r and C_r, as shown in Fig. 1) is required to absorb the second-order resonating power, which descends system reliability, increases costs, and decreases the power density of the traction drive system. To replace the dedicated passive *LC* resonance filter in the HEMU, the BBDC is utilized in this article. When $K1$ is ON, the BBDC is employed to power the inverter–motor system in the battery mode. While $K1$ is OFF, the BBDC tends to decouple the resonating power $p_{2\text{-ripple}}$ into the nondedicated *LC* branches L_{cs} and C_{cs} in the catenary mode. The on-board battery can be charged not only in the regenerative braking state but also at the railway station or train depot while the ac source is available, and motors are static; thus, the performance of the motors will not be affected. Compared with electric vehicles, the running routes and timetables of the HEMU are fixed in advance. Therefore, the energy management strategy is easy to implement, and the on-board battery can always be in a proper state of charge to achieve the former functions of operating on nonelectrified routes and/or emergency situations. Consequently, the dedicated passive *LC* resonance filter is removed, and the utilization of the BBDC can be improved.

B. Power Coupling Feature of the BBDC

As shown in Fig. 1, the direction and value of the power flowing in passive components (L_{cs} and C_{cs}) can be controlled by the switches $S1$ and $S2$ to achieve complementary to the resonating power $p_{2\text{-ripple}}$, thereby avoiding the second-order voltage fluctuation in the dc link. In the steady state (assuming no loss, no switching ripples), the current i_{cs} through the filter inductor L_{cs} must be ac components without dc component, and the fundamental angular frequency of i_{cs} is 2ω (twice the grid angular frequency). As the BBDC is with a half-bridge structure, there must be a positive dc-bias voltage across the decoupling capacitor C_{cs}. Assuming that the second-order resonating power is totally compensated by the power p_{LC} flowing in the series branches L_{cs} and C_{cs}, the following equation can be obtained:

$$\begin{aligned} p_{2-\text{ripple}} &= p_{LC} = i_{cs} u_{\text{in}} \\ &= L_{cs} \frac{d i_{cs}}{dt} i_{cs} + \left(U_{cs} + \frac{1}{C_{cs}} \int i_{cs} dt \right) i_{cs} \end{aligned} \tag{4}$$

where u_{in} is the voltage across the series branches *Lcs* and *Ccs*, and U_{cs} is the dc-bias voltage across C_{cs}. Clearly, i_{cs} can be decomposed into the Fourier series as

$$i_{cs} = \sum_{k=1}^{n} A_{2k} \sin(2k\omega t + \theta_{2k}) \tag{5}$$

where n represents the highest order, and A_{2k} and θ_{2k} are the amplitude and phase of the k-order current in i_{cs}, respectively. Hence, (4) and (5) yield $p_{2\text{-ripple}}$ as

$$\begin{aligned} p_{2-\text{ripple}} = & \left\{ \begin{array}{l} L_{cs} \left[2\omega \left(\sum_{k=1}^{n} k A_{2k} \sin\left(2k\omega t + \theta_{2k} + \frac{\pi}{2}\right) \right) \right] \\ + \frac{1}{C_{cs}} \left[\frac{1}{2\omega} \left(\sum_{k=1}^{n} \frac{1}{k} A_{2k} \sin\left(2k\omega t + \theta_{2k} - \frac{\pi}{2}\right) \right) \right] \end{array} \right\} \\ & \times \left[\sum_{k=1}^{n} A_{2k} \sin(2k\omega t + \theta_{2k}) \right] \\ & + U_{cs} \left[\sum_{k=1}^{n} A_{2k} \sin(2k\omega t + \theta_{2k}) \right]. \end{aligned} \tag{6}$$

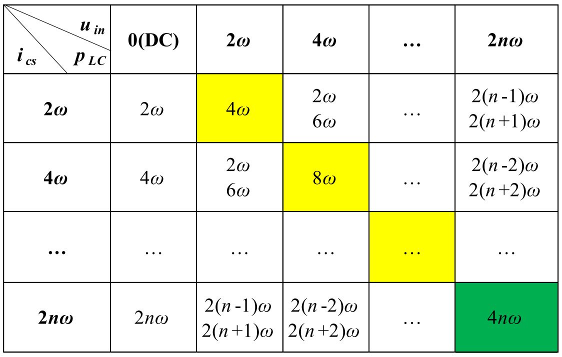

i_{cs} \ u_{in}, p_{LC}	**0(DC)**	**2ω**	**4ω**	**…**	**$2n\omega$**
2ω	2ω	🟨 4ω	2ω 6ω	…	$2(n-1)\omega$ $2(n+1)\omega$
4ω	4ω	2ω 6ω	🟨 8ω	…	$2(n-2)\omega$ $2(n+2)\omega$
…	…	…	…	🟨 …	…
$2n\omega$	$2n\omega$	$2(n-1)\omega$ $2(n+1)\omega$	$2(n-2)\omega$ $2(n+2)\omega$	…	🟩 $4n\omega$

Fig. 2. Power coupling feature of the BBDC.

It can be easily known that the sinusoidal terms on the right side of (6) are distributed as Fig. 2. The result of the intersection of the rows and column in Fig. 2 can be expressed as that the production of a sinusoidal term at an angular frequency of $2k_1\omega$ and a sinusoidal term at an angular frequency of $2k_2\omega$ ($k_1 \geq k_2$) is equal to the sum of a sinusoidal term at an angular frequency of $2\omega(k_1-k_2)$ and a sinusoidal term at an angular frequency of $2\omega(k_1+k_2)$. Especially when k_1 is equal to k_2, the results will be only one sinusoidal term at an angular frequency of $4k_1\omega$ without dc component as u_{in} and i_{cs} are orthogonal at the same frequency (shown in the colored part of Fig. 2). Merging all sinusoidal terms at the same angular frequency (2ω, 4ω, 6ω, …, $4k\omega$ when $n = k$) together, (6) can be simplified as follows:

$$p_{2-\text{ripple}} = \sum_{k=1}^{2n} A'_{2k} \sin\left(2k\omega t + \theta'_{2k}\right) \tag{7}$$

where A'_{2k} and θ'_{2k} are the amplitude and phase of the k-order resonating power in p_{LC}, and $A'_{4k} = 0.5A2\ 2k[2k\omega L_{cs}-1/(2k\omega C_{cs})]$ (shown in the green part of Fig. 2). Based on (5) and (7), there are $A_{2k} = \cdots = A_6 = A_4 = 0$ and $2\omega L_{cs} = 1/(2\omega C_{cs})$. Thus, i_{cs} can be expressed as

$$i_{cs} = A_2 \sin\left(2\omega t + \theta_2\right) \tag{8}$$

where $\theta_2 = \theta$, $A_2 = P_{2\text{-peak}}/U_{cs}$, and $1/(L_{cs}C_{cs}) = 4\omega^2$.

The above derivation illustrates the power coupling feature of the BBDC: if the resonance frequency of the nondedicated *LC* branch is not 2ω, the higher order resonating power will be introduced, while the low-order resonating power is canceled.

III. PARAMETERS AND CONTROLLER DESIGN

Normally, the power coupling feature can be ignored due to the small inductance of the filter inductor, and only the decoupling capacitor is used for resonating power storage. As for the high-power applications, the large inductance will result in both large voltage drop and huge stored energy. Consequently, these factors must be considered for both parameters and controller design in the HEMU.

A. Resonating Power Spectrum Shifting

According to the analysis above, the compensation of the second-order resonating power can be realized as long as i_{cs} is an ac term as

$$i_{cs} = A_2 \sin\left(2\omega t + \theta_2\right) \tag{9}$$

where $A_2 = P_{2\text{-peak}}/U_{cs}$ and $\theta_2 = \theta$. Therefore, p_{LC} can be yielded by (4) and (9) as

$$\begin{aligned} p_{LC} = {} & A_2 U_{cs} \sin\left(2\omega t + \theta_2\right) \\ & + A_2^2 \left(2\omega L_{cs} - \frac{1}{2\omega C_{cs}}\right) \sin\left(4\omega t + 2\theta_2\right). \end{aligned} \tag{10}$$

Obviously, the fourth-order resonating power is introduced because of the power coupling feature of the BBDC. Furthermore, the fourth-order current can be superimposed into i_{cs}. Therefore, i_{cs} is given by

$$i_{cs} = A_2 \sin\left(2\omega t + \theta_2\right) + A_4 \sin\left(4\omega t + \theta_4\right) \tag{11}$$

where $\theta_2 = \theta$ and $\theta_4 = 2\theta$. Consequently, p_{LC} can be yielded by (4) and (11) as

$$\begin{aligned} p_{LC} = {} & A'_2 \sin\left(2\omega t + \theta_2\right) + A'_4 \sin\left(4\omega t + 2\theta_2\right) \\ & + A'_6 \sin\left(6\omega t + 3\theta_2\right) + A'_8 \sin\left(8\omega t + 4\theta_2\right). \end{aligned} \tag{12}$$

According to Fig. 2, there is no doubt that $A'_2 = P_{2\text{-peak}}$ and $A'_4 = 0$ can be realized under certain A_2 and A_4. Therefore, not only the second-order resonating power can be eliminated but also the fourth-order resonating power can be canceled. Although the sixth- and eighth-order resonating power is introduced in this case, these components are under smaller amplitude with higher frequency; thus, the dc-link voltage will be smoother. The voltage ripples introduced by the sixth- and eighth-order resonating power can be easily derived as follows:

$$v_d = -\frac{A'_6 \cos\left(6\omega t + 3\theta_2\right)}{6\omega C_d U_d} - \frac{A'_8 \cos\left(8\omega t + 4\theta_2\right)}{8\omega C_d U_d} \tag{13}$$

where U_d is the dc-bias voltage of the dc-link voltage u_d, and

$$A'_6 = \frac{A_2^3}{4U_{cs}} \left(2\omega L_{cs} - \frac{1}{2\omega C_{cs}}\right) \left(2\omega L_{cs} + \frac{3}{4\omega C_{cs}}\right)$$

$$A'_8 = \frac{A_2^4}{8U_{cs}^2} \left(2\omega L_{cs} - \frac{1}{2\omega C_{cs}}\right)^2 \left(4\omega L_{cs} - \frac{1}{4\omega C_{cs}}\right).$$

Apparently, it is possible to superimpose the sixth- and eighth-order current to decouple the sixth- and eighth-order resonating power and further shift the spectrum of the resonating power to a higher order region. However, the voltage ripples reduction will be small, and it is challenging to track the higher order signals with low switching frequency.

B. Parameters Design

The BBDC designed in this article can not only decouple the resonating power but also charge and discharge the battery. Therefore, the parameters design must consider the requirements of the multifunction of the BBDC. Besides, it is necessary to take into account the power coupling feature and the voltage drop across the filter inductor. Consequently, the parameters design, in this case, must be different from the existing cases.

1) Design and Influence of Filter Inductor: In battery mode, the large current ripples will cause heating and accelerate battery aging [34], [35]. Therefore, it is necessary to consider the current ripples of the battery to design the filter inductor L_{cs}. Assuming that the battery voltage is U_{bat}, the duty cycle of $S1$ can be expressed as

$$D_b = \frac{U_{\text{bat}}}{U_d}. \tag{14}$$

Thus, with the fixed switching period T_s, the peak-to-peak value of the current ripples is derived as

$$\Delta I_{\text{battery}} = \frac{U_d - U_{\text{bat}}}{L_{cs}} D_b T_s. \tag{15}$$

With the limited peak-to-peak value of the current ripples $\Delta I_{\text{battery}}$, L_{cs} should satisfy the following limitation:

$$L_{cs} \geq \frac{U_d - U_{\text{bat}}}{\Delta I_{\text{battery}}} D_b T_s = \frac{U_d - U_{\text{bat}}}{\Delta I_{\text{battery}}} \frac{U_{\text{bat}}}{U_d} T_s. \tag{16}$$

The current ripple $\Delta I_{\text{battery}}$ is limited to 100 A in consideration of the heat dissipation design of the battery; thus, L_{cs} can be calculated by (16) as 3.67 mH. Eventually, L_{cs} is selected as 4 mH for increasing the amplitude margin of battery current in the following simulations and experiments. If the influence of filter inductor L_{cs} is not considered, the second-order resonating power will be totally compensated by the decoupling capacitor C_{cs}, and the following equation is obtained:

$$p_{2-\text{ripple}} = u_{cs} C_{cs} \frac{du_{cs}}{dt}. \tag{17}$$

Based on (17), u_{cs} and i_{cs} are derived as follows:

$$u_{cs} = \sqrt{\frac{P_{2-\text{peak}}}{C_{cs}\omega}\left[K - \cos(2\omega t + \theta)\right]} \tag{18}$$

$$i_{cs} = \frac{P_{2-\text{peak}} \sin(2\omega t + \theta)}{\sqrt{\frac{P_{2-\text{peak}}}{C_{cs}\omega}\left[K - \cos(2\omega t + \theta)\right]}} \tag{19}$$

where K is a constant that should be more than 1.0. Therefore, the power in filter inductor L_{cs} can be yielded as

$$p_{FI} = L_{cs} \frac{di_{cs}}{dt} i_{cs}. \tag{20}$$

Such a power p_{FI} will cause the dc-link voltage to fluctuate with high amplitude, and Fig. 3 shows the fast Fourier transform (FFT) analysis of the dc-link voltage ripples introduced by the resonating power p_{FI} while $K = 1.5$. As the inductance of the filter inductor is so high, it will significantly deteriorate the power-decoupling performance.

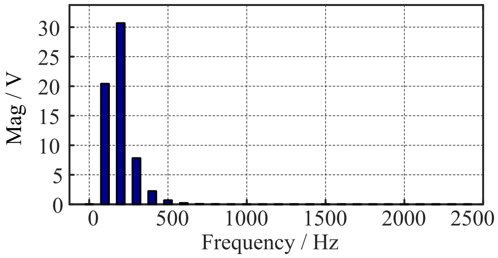

Fig. 3. FFT analysis of the dc-link voltage ripples introduced by p_{FI} while $K = 1.5$.

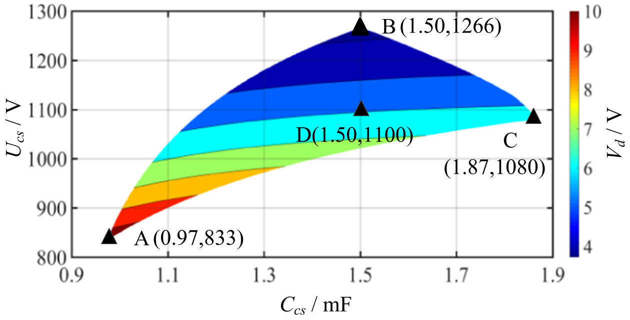

Fig. 4. Amplitude of dc-link voltage fluctuation V_d introduced by higher order resonating power within the range of C_{cs} and U_{cs}.

2) Design of C_{cs}: The objective of designing C_{cs} is to meet the requirement for resonating power decoupling. To achieve a minimum decoupling capacitor, the decoupling capacitor C_{cs} should be fully charged and discharged in one power cycle (the minimum across the capacitor is zero, and the maximum value is the dc-link voltage) [17]. However, the current of the filter inductor i_{cs} will be too sharp to be tracked with the physical limitation of passive components under the minimum decoupling capacitor. Therefore, considering the physical limitation of the BBDC (i.e., the voltage across the filter inductor), there are the constrictions as (assuming no loss, no switching ripples)

$$0 \leq dU_d = L_{cs}\frac{di_{cs}}{dt} + \frac{1}{C_{cs}} \int i_{cs} dt + U_{cs} \leq U_d \tag{21}$$

where d is the duty cycle of $S1$ as a function of time. Meanwhile, to avoid large volume (the higher the voltage stress is, the larger the volume of C_{cs} will be) and to simplify the design of overvoltage protection, the voltage of the decoupling capacitor C_{cs} should not be too high with the limitation as

$$U_{cs} + \frac{1}{C_{cs}} \int i_{cs} dt \leq U_d. \tag{22}$$

Considering the power coupling feature of the BBDC, the range of decoupling capacitor C_{cs} and the dc-bias voltage U_{cs} can be obtained according to (11), (12), (21), and (22), as shown in Fig. 4. Different ranges in Fig. 4 show the amplitude of the dc-link voltage fluctuation introduced by the higher order resonating power with different values of C_{cs} and U_{cs}, which can be calculated by (13). It shows that the amplitude of the dc-link voltage fluctuation V_d increases with the increase of C_{cs} and the decrease of U_{cs}, and the minimum value of V_d is obtained at point B. To ensure that the power decoupling can still be realized when the HEMU traction drive system is slightly overloaded, point D, where $C_{cs} = 1.5$ mF and $U_{cs} = 1100$ V, is selected in the following analysis.

3) Current and Voltage Stress Analysis: When 4QC operates at rated power with unit power factor, according to (2), (3), and the parameters in Table I, the magnitude of the resonating power generated by one 4QC can be calculated as

$$P_{2-\text{peak}} = 491\,\text{k}VA. \tag{23}$$

According to (11) and (12), the maximum decoupling capacitor current $I_{cs\max}$ and voltage $U_{cs\max}$ at rated power are derived as follows:

$$I_{cs\,\max} = \max\begin{pmatrix} A_2\sin(2\omega t + \theta_2) \\ +A_4\sin(4\omega t + \theta_4)\end{pmatrix} = 404\ \text{A} \tag{24}$$

$$U_{cs\,\max} = U_{cs} + \max\left(\frac{1}{C_{cs}}\int\begin{pmatrix} A_2\sin(2\omega t + \theta_2) \\ +A_4\sin(4\omega t + \theta_4)\end{pmatrix}dt\right) = 1545\ \text{V}. \tag{25}$$

The root-mean-square value $I_{cs\text{RMS}}$ at rated power is as follows:

$$I_{cs\text{RMS}} = \frac{A_2 + A_4}{\sqrt{2}} = 311\ \text{A}. \tag{26}$$

The current of the battery at rated power is calculated as follows:

$$I_{\text{battery}} = \frac{P_{\text{rated}}}{U_{\text{bat}}} = 418\ \text{A} \tag{27}$$

where P_{rated} is 460 kW, as given in Table I. Equations (26) and (27) show that the heating loss of the filter inductor L_{cs} and IGBT bridge arm in power-decoupling mode are smaller than that in battery mode. Equations (24) and (27) indicate that the maximum current in power-decoupling mode still meets the requirements designed for battery mode.

C. Direct Resonance Control Method

The power coupling feature shows the impossibility of canceling out the resonating power totally. Fortunately, the resonating power spectrum shifting feature indicates that the dc-link voltage can be smoother as long as the low-order resonating power can be eliminated. Therefore, according to the automatic-power-decoupling principle [20] and the resonating power spectrum shifting feature, a controller to suppress the second- and fourth-order dc-link voltage ripples is needed. Besides, it should be noted that the series branches L_{cs} and C_{cs} are without any damping resistance; thus, the state feedback is required to increase the damping ratio. What is more, it is necessary to maintain the dc-bias voltage U_{cs} with the value of 1100 V according to the parameters design above. Therefore, the direct resonance control method is proposed to decouple the low-order resonating power with good performance, as shown in Fig. 5.

The current is fed back with the coefficient k_i to damp the series *LC* branch; thus, its high resonance peak can be shaped. As for u_{cs}, the PI controller G_v is used to achieve the error-free tracking for the dc component U_{cs} and can be described as

$$G_{\text{v}} = k_{pv} + \frac{k_{\text{iv}}}{s} \tag{28}$$

where k_{pv} and k_{iv} are the proportional coefficient and integral coefficient, respectively. The resonance controllers at 100 Hz and 200 Hz in parallel are utilized for u_d to force the second- and fourth-order dc-link voltage ripples to be zero as the second- and fourth-order resonating power is decoupled by the series branches L_{cs} and C_{cs}, and they are given as

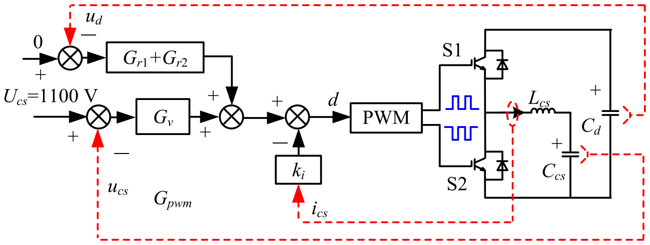

Fig. 5. Direct resonance control method.

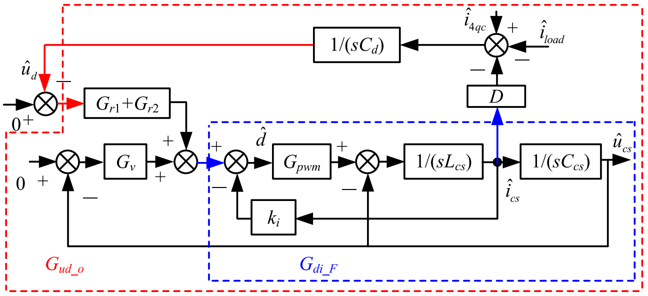

Fig. 6. Small-signal model of the control system.

$$G_{r1} = \frac{k_{r1}s}{s^2 + 4\omega^2} \tag{29}$$

$$G_{r2} = \frac{k_{r2}s}{s^2 + 16\omega^2} \tag{30}$$

where k_{r1} and k_{r2} are the coefficients for G_{r1} and G_{r2}. In the low-power applications, the voltage loop of u_d can be connected in series before the voltage loop of u_{cs} because of the high control bandwidth, and the control parameters can be designed easily. However, due to the low switching frequency and the low resonance frequency of the nondedicated *LC* branch of the BBDC (65 Hz), the control bandwidth of the voltage loop of u_{cs} is limited. Therefore, the voltage loop of u_d is connected in parallel with the voltage loop of u_{cs} directly. Consequently, the control performance will be enhanced because of the reduced control loops.

D. Controller Parameters Design

According to Fig. 1, the dc-link voltage u_d can be expressed as

$$u_d = \frac{-i_{cs}d + i_{4\text{qc}} - i_{\text{load}}}{C_d s} \tag{31}$$

where $i_{4\text{qc}}$ is the current that the 4QC inputs to the dc link, and i_{load} is the current of loads. As i_{cs} is without the dc component, the small-signal transfer function of $\hat{u}_d$ can be obtained

$$\hat{u}_d = \frac{-D\hat{i}_{cs} + \hat{i}_{4\text{qc}} - \hat{i}_{\text{load}}}{C_d s} \tag{32}$$

where $D = U_{cs}/U_d = 0.67$. The small-signal model of the control system is demonstrated in Fig. 6, and G_{pwm} is the transfer

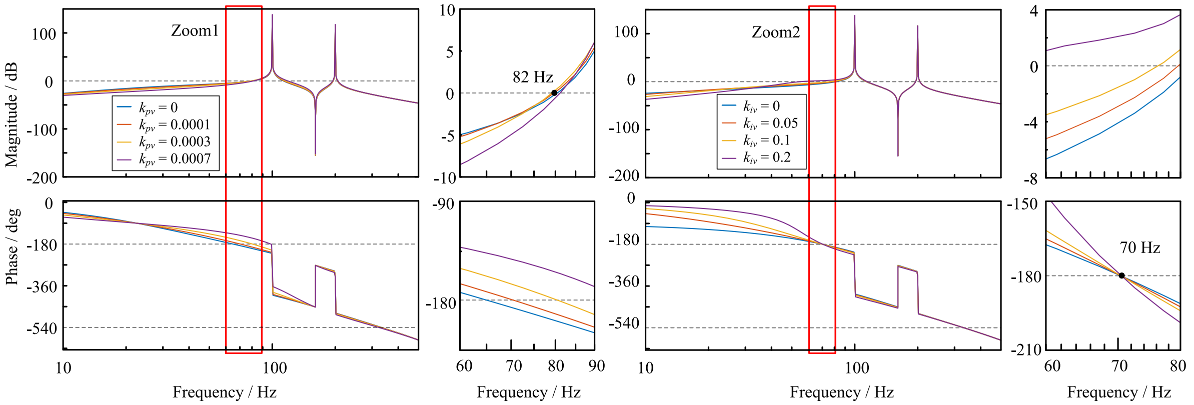

(a) (b) (c) (d)

Fig. 7. Bode diagrams of $G_{ud\text{-}o}$. (a) Under k_{iv}= 0.05 and k_{pv} ranged from 0 to 0.0007. (b) In Zoom1. (c) Under k_{pv}= 0.0001 and k_{iv} ranged from 0 to 0.2. (d) In Zoom2.

function for the pulsewidth modulation (PWM)

$$G_{\text{pwm}} = U_d e^{-1.5sT_c} \tag{33}$$

where T_c is the control period and is half of the switching period T_s. After the current feedback is applied, the closed current-loop transfer function is as follows:

$$G_{di\_F} = \frac{G_{\text{pwm}} C_{cs} s}{L_{cs} C_{cs} s^2 + k_i G_{\text{pwm}} C_{cs} s + 1}. \tag{34}$$

As the resonance frequency of the series LC branch is as low as 65 Hz, G_{pwm} will result in a small phase delay at such frequency. Therefore, G_{pwm} is simplified as U_d for the design of k_i, and the damping ratio is set as 0.707. Thus, k_i can be obtained with the value of 0.0014. The parameters design for G_v can be easily achieved according to the conventional design principle of the PI controller. However, it should be noted that the stability of the closed voltage loop of u_d can be affected by G_v. Therefore, G_v must be designed carefully. According to Fig. 6, the transfer function of the voltage loop of u_d in an open-loop manner can be derived as

$$G_{ud\_o} = -\frac{D}{C_d} \frac{G_{\text{pwm}} C_{cs} (G_{r1} + G_{r2})}{s^2 L_{cs} C_{cs} + s k_i G_{\text{pwm}} C_{cs} + G_v G_{\text{pwm}} + 1}. \tag{35}$$

Fig. 7 shows the bode diagram of G_{ud_o} while k_{pv} and k_{iv} are under different values. It can be seen that the frequency responses of $G_{ud\ \_o}$ at 100 and 200 Hz are almost the same with different k_{pv} and k_{iv}. Therefore, k_{r1} and k_{r2} are set as 0.9 and 0.8 for high gain at 100 and 200 Hz, and the parameters design for G_v can be simplified. It is well known that the control system is stable in a closed-loop manner if the phase of the control system in an open-loop manner does not cross (2k+1)180° (k is an integer) within the region where the gain is above 0 dB. As seen from Fig. 7(a) and (c), it is obvious that the phase will not cross −540° near 200 Hz. Hence, to stabilize the voltage loop of u_d, the phase cannot cross −180° near 100 Hz. In Fig. 7(a), k_{iv} is fixed at 0.05, and k_{pv} is ranged from 0 to 0.007 to show the influence of k_{pv} on the bode diagram of $G_{ud\ \_o}$. Fig. 7(b) shows the enlarged view of Zoom1 in Fig. 7(a). As k_{pv} increases, the region where the gain is above 0 dB is almost the same. However, the cross frequency increases with k_{pv}, and the critical stable cross frequency is about 82 Hz. In Fig. 7(c), k_{pv} is fixed at 0.0001, and k_{iv} is ranged from 0 to 0.2 to show the influence of k_{iv} on the bode diagram of $G_{ud\ \_o}$. Fig. 7(d) shows the enlarged view of Zoom2 in Fig. 7(c). Different from Fig. 7(b), the cross frequency remains constant with the value of 70 Hz while the gain increases with k_{iv}, resulting in the phase crosses 180° above 0 dB. Therefore, k_{pv} and k_{iv} should be small enough to maintain the stability of the voltage loop of u_d. Thus, to compromise the stability of the voltage loop of u_d and the performance of the voltage loop of u_{cs}, k_{pv} and k_{iv} are set as 0.0001 and 0.05, respectively.

Based on the power coupling and spectrum shifting feature of the BBDC, the second- and fourth-order resonating power is regulated by the direct resonance control method. Although the higher order resonating power is generated, it will have little influence on the dc-link voltage. Therefore, the dc-link voltage can be smoother. The inner current feedback damps the plant model; thus, the stability of the control system can be enhanced. Besides, the parameters tunning method for the controller design can be applied easily. Compared with the direct-power-decoupling control methods, the proposed method is more robust and simpler. Due to the low switching frequency and the low resonance frequency of the nondedicated LC branch in the BBDC, the system is of low control bandwidth. Therefore, the dynamic performance of the control system can be slow. However, it still can meet the requirements for the HEMU.

IV. SIMULATIONS AND EXPERIMENTAL VERIFICATION

A. *Simulations' Results*

In simulations, one 4QC operates with double BBDCs, and the value of the dc-link capacitor is 4 mF. The midpoint of one BBDCs bridge arm is connected with L_{load} and R_{load} series branch ($L_{\text{load}} = 4$ mH and $R_{\text{load}} = 1.5\ \Omega$) to simulate loads by controlling the duty cycle of the upper IGBT (D_{load}). In addition, another BBDC is used for power decoupling while $C_{cs} = 1.5$ mF and $L_{cs} = 4$ mH according to the previous parameters design. The simulation model is built by MATLAB/Simulink, and a virtual DSP, including timing interruption, Analog-to-Digital

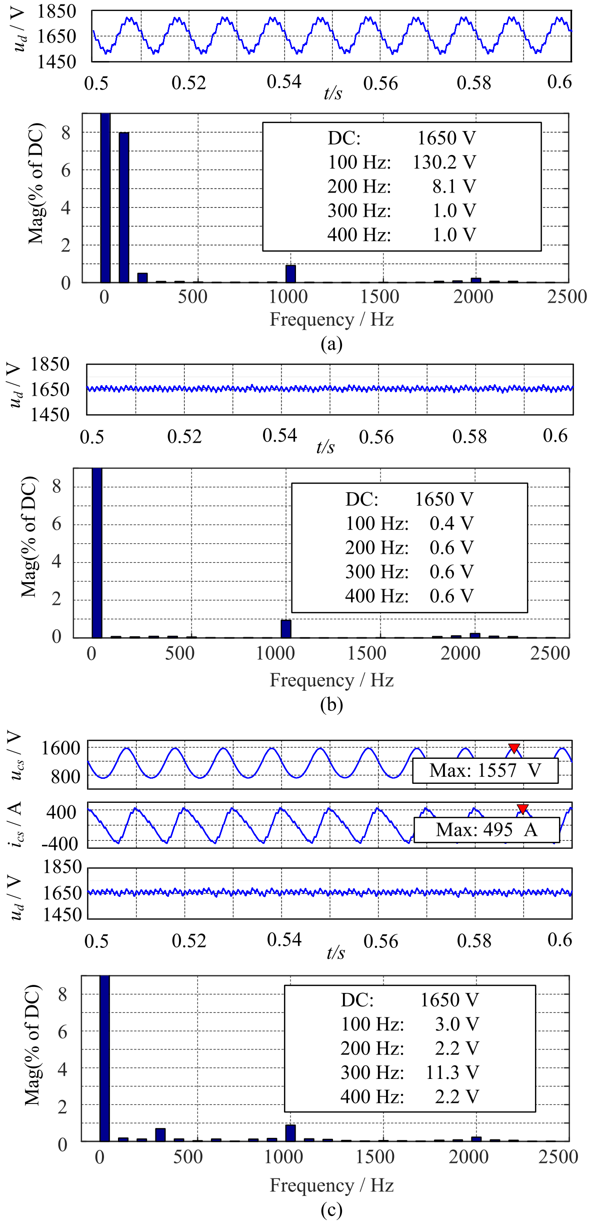

Fig. 8. Simulation waveforms and FFT analysis of the dc-link voltage. (a) Without the power-decoupling method. (b) With the PLC method. (c) With the UBBDC method.

Converter (ADC), Enhanced Pulse Width Modulator (EPWM), etc., is programmed by S-Function. D_{load} is set to be 0.5 to simulate the rated power.

Fig. 8(a) presents the dc-link voltage u_d across the dc-link capacitor without the power-decoupling method and the FFT analysis of it. The amplitude of the voltage ripple at 100 Hz is as high as 130.2 V, and the motors' performance will be significantly affected. The simulation results in Fig. 8(b) show no voltage ripples at low frequency with the PLC method. Fig. 8(c) shows the effectiveness of the power-decoupling method with the UBBDC method, and the voltage ripples at 100 and 200 Hz on the dc-link capacitor are almost eliminated. In comparison, the voltage ripples at 300 and 400 Hz increase slightly. The results are consistent with the analysis above. It can be seen that the voltage fluctuation reduction on the dc-link capacitor by utilizing the BBDC is very close to that by using the PLC method.

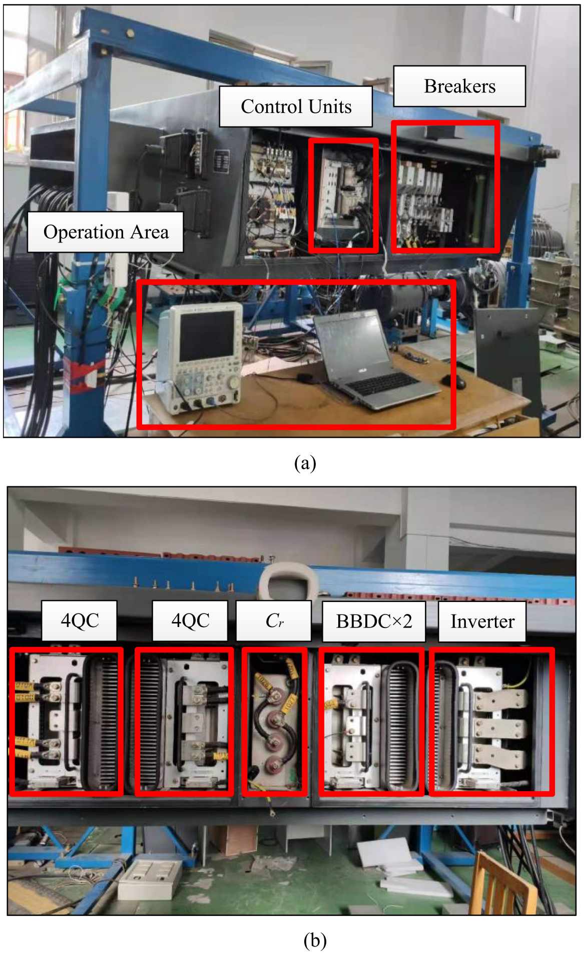

Fig. 9. Test platform of the HEMU traction drive system. (a) Front part of the HEMU traction drive system. (b) Back part of the HEMU traction drive system.

B. Experimental Results

To verify the proposed power-decoupling method by utilizing the BBDC, experiments are implemented based on the test platform of the HEMU traction drive system, as shown in Fig. 9. In the front of the HEMU traction drive system, as shown in Fig. 9(a), control units and breakers can be seen straight. By operating the host computer in the operation area, the data can be sent to control units. Hence, the parameters used for the control method can be regulated online to accelerate the control system's design process. In the back of the HEMU traction drive system, as shown in Fig. 9(b), there are capacitor C_r for the passive *LC* resonance filter and four power modules in which the IGBT bridge arms, heat sink, driver, and the dc-link capacitor valued 2 mF are integrated together. As can be seen from Fig. 9(b), double power modules are used for 4QCs, and one power module is used for double BBDCs, while one power module is used for the inverter to drive motors. Other components, such as fans, L_r, and L_{cs}, are inside the HEMU traction drive system.

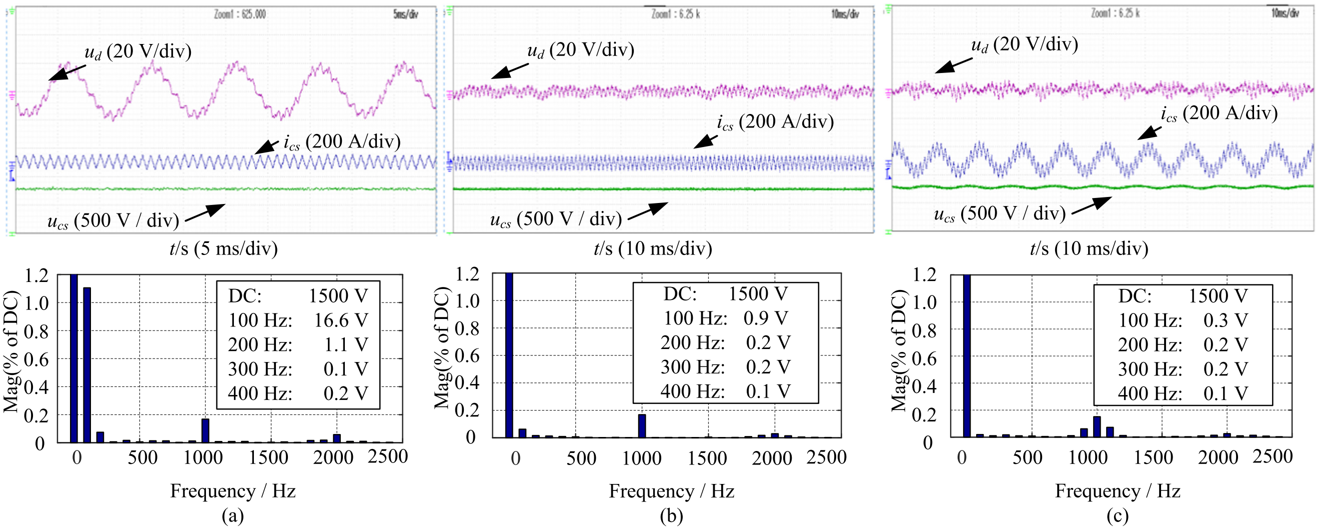

Fig. 10. Experimental waveforms and FFT analysis of the dc-link voltage. (a) Without the power-decoupling method. (b) With the PLC method. (c) With the UBBDC method.

The experimental configuration is consistent with that in the simulations, while R_{load} is adjusted to be 11 Ω, and the dc voltage is set to be 1500 V for obvious voltage ripples observation.

1) Steady Experimental Results: Because the power level of the test platform is limited, D_{load} is set to be 0.5, and the power is about 50 kW. In Fig. 10(a) and (b), the resonance controller $G_{r1}+G_{r2}$ is disabled to keep the voltage of the decoupling capacitor as the dc value. Fig. 10(a) shows the experimental results of the dc-link voltage u_d without power-decoupling method and the FFT analysis of it. The amplitude of the voltage ripple at 100 Hz is 16.6 V. Fig. 10(b) shows the experimental results of the dc-link voltage u_d with the PLC method. There are still voltage ripples at 100 Hz with small amplitude because the value of the capacitor C_r has attenuated over time, and the second-order resonating power cannot be decoupled totally. With the UBBDC method, the voltage ripples decrease sharply, and the main component among the voltage ripples is the switching ripple, as shown in Fig. 10(c). The FFT analysis of the dc-link voltage shows that the voltage ripples at 100 and 200 Hz are eliminated, and the voltage ripples at 300 and 400 Hz do not vary much because of the low-power level. It can be seen from Fig. 10 that the effectiveness of power decoupling by utilizing the BBDC is close to that by using the PLC method.

2) Dynamic Experimental Results: To further test the performance of the power-decoupling method with the PLC method and the UBBDC method, the motor is running at 95 Hz (i_a is the motor's current), and the dynamic experiments are implemented, as shown in Figs. 11 and 12. Fig. 11(a) shows the overall dynamic waveforms with the PLC method, and Fig. 11(b) and (c) shows the enlarged views of Zoom1 and Zoom2 in Fig. 11(a) when the loads suddenly changed (50 kW). It can be seen that the 4QC needs about 300 ms to regulate the dc-link voltage to the steady-state value, and the resonating power is eliminated within 50 ms. Besides, there is still a voltage ripple at 100 Hz with a small amplitude because of the varied value of C_r over time, resulting in slightly current harmonics of the motor. Fig. 12(a) shows the overall waveforms of the experiments with the UBBDC method, and Fig. 12(b)–(d) shows the enlarged views of Zoom1, Zoom2, and Zoom3 in Fig. 12(a), respectively. Fig. 12(b) shows the dynamic waveforms before and after the power-decoupling method is adopted. It can be seen that the low harmonics of the motor current are significantly suppressed after utilizing the BBDC to decouple the resonating power. Fig. 12(c) shows the dynamic waveform when the loads suddenly decrease (50 kW). It can be seen that the 4QC needs about 200 ms to regulate the dc-link voltage to the steady-state value, and

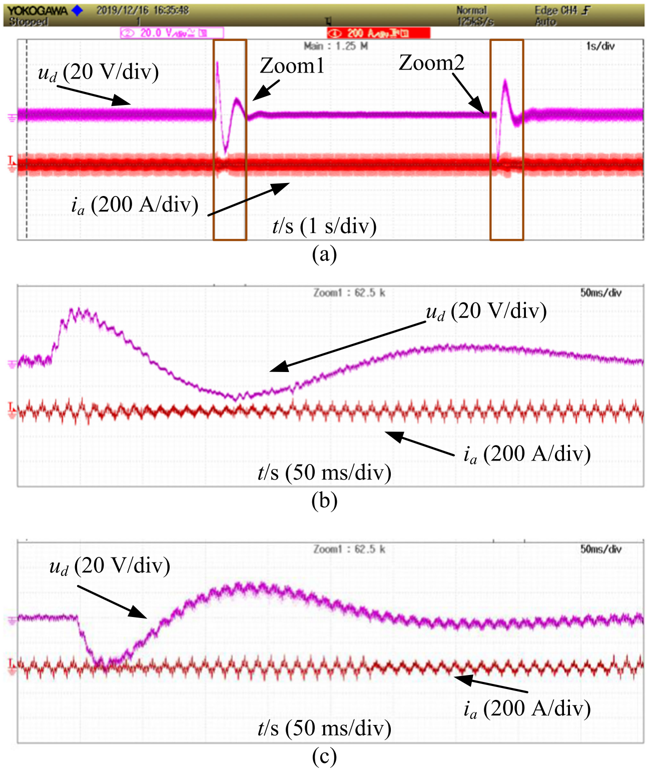

Fig. 11. Dynamic experiments with the PLC method. (a) Overall waveforms. (b) Loads suddenly decrease in Zoom1. (c) Loads suddenly increase in Zoom2.

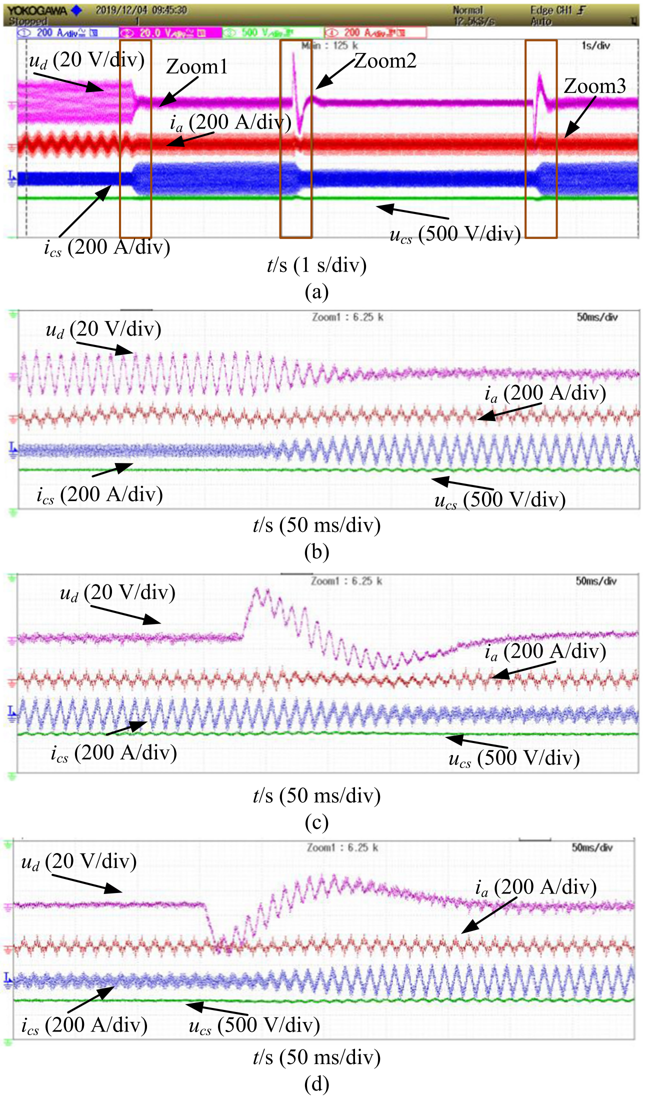

(a)

(b)

(c)

(d)

Fig. 12. Dynamic experiments with the UBBDC method. (a) Overall waveforms. (b) Before and after the BBDC is adopted in Zoom1. (c) Loads suddenly decrease in Zoom2. (d) Loads suddenly increase in Zoom3.

the resonating power is eliminated by power decoupling within 150 ms. Similarly, when the loads suddenly increase (50 kW), as shown in Fig. 12(d), the adjust time for power decoupling is also less than that for the 4QC. Obviously, the dynamic performance of the whole control system is good. Comparing Fig. 11 with Fig. 12, it can be seen that the overall dynamic performance with the UBBDC method is almost the same as that with the PLC method.

C. Discussion

In simulations, the maximum voltage of the decoupling capacitor is 1574 V, as shown in Fig. 8(c), which is nearly consistent with (25). Because the switching ripples are not considered in (24), the maximum current of the decoupling capacitor in Fig. 8(c) (495 A) is much higher, which is still lower than that in battery mode (418 A + 100 A). The results show that the BBDC designed for the battery mode can still be applied to the power-decoupling mode. The amplitude of the voltage ripples at 300 and 400 Hz, as shown in Fig. 8(c), is small, which almost meets the numerical results in Fig. 4. Thereby, the parameter design is verified. Although the experiments at rated power cannot be carried out, the steady and dynamic performance still shows that the control system works well in practice. The dynamic response shown in experiments is not as good as that in low-power applications due to narrow control bandwidth. However, it can be accepted for EMUs.

As mentioned above, the power-decoupling effect under PLC mode can be degraded because the resonance frequency of the passive *LC* filter is shifted over time. Besides, once the passive *LC* filter is installed, it can only filter out the resonating power at a fixed frequency. In some countries, e.g., Japan, the grid frequency can be 50 or 60 Hz, which limits the use of the PLC method. As for the UBBDC method, it can adapt to such circumstances more flexibly by adjusting the resonance frequency of G_{r1} and G_{r2}. Therefore, the UBBDC method has better adaptability compared with the PLC method.

V. CONCLUSION

In this article, utilizing the BBDC in the HEMU is proposed to decouple the resonating power; thus, the conventional passive *LC* resonance filter is completely replaced. The parameters are specially designed for the BBDC by considering the requirements for the battery mode and the power decoupling. Based on the power coupling phenomenon and spectrum shifting feature of the BBDC, the direct resonance control method is proposed to decouple the low-order resonating power, and the controller parameters design is analyzed. The simulations and experimental results show that the effectiveness of the power-decoupling method by utilizing the BBDC is close to that by using the passive *LC* resonance filter both in steady and transient states.

REFERENCES

[1] Y. Lei, K. Wang, L. Zhao, Q. Ge, Z. Li, and Y. Li, “An improved torque and current pulsation suppression method for railway traction drives under fluctuating DC-link voltage,” *IEEE Trans. Power Electron.*, vol. 33, no. 10, pp. 8565–8577, Oct. 2018.

[2] A. Kimura, “Frequency domain analysis of beat-less control method for converter-inverter driving systems applied to AC electric cars,” *IEEJ Trans. Ind. Appl.*, vol. 128, no. 11, pp. 1269–1274, Jan. 2008.

[3] W. Song, K. Smedley, X. Feng, and P. Sun, “One-cycle control of induction machine traction drive for high speed railway—Part I: Multi-pulse width modulation region,” in *Proc. 36th Annu. Conf. IEEE Ind. Electron. Soc.*, 2010, pp. 2346–2351.

[4] H. Ouyang, K. Zhang, P. Zhang, Y. Kang, and J. Xiong, “Repetitive compensation of fluctuating DC link voltage for railway traction drives,” *IEEE Trans. Power Electron.*, vol. 26, no. 8, pp. 2160–2171, Aug. 2011.

[5] B. Gou, X. Feng, W. Song, K. Han, and X. Ge, “Analysis and compensation of beat phenomenon for railway traction drive system fed with fluctuating DC-link voltage,” in *Proc. 7th Int. Power Electron. Motion Control Conf.*, 2012, pp. 654–659.

[6] G. W. Chang, H.-W. Lin, and S.-K. Chen, “Modeling characteristics of harmonic currents generated by high-speed railway traction drive converters,” *IEEE Trans. Power Del.*, vol. 19, no. 2, pp. 766–773, Apr. 2004.

[7] D. Ronanki and S. S. Williamson, “Submodule power balancing control of modular multilevel converters under capacitor degradation,” *IET Power Electron.*, vol. 13, no. 14, pp. 3032–3043, Aug. 2020.

[8] A. Goodarzi, M. Allahbakhshi, M. Tajdinian, and M. Popov, “Multi-criteria protection scheme for online element failure detection in shunt capacitor banks,” *IET Gener., Transmiss. Distrib.*, vol. 14, no. 19, pp. 4152–4163, Oct. 2020.

[9] Y. Sun, Y. Liu, M. Su, W. Xiong, and J. Yang, "Review of active power decoupling topologies in single-phase systems," *IEEE Trans. Power Electron.*, vol. 31, no. 7, pp. 4778–4794, Jul. 2016.

[10] M. A. Vitorino, L. F. S. Alves, R. Wang, and M. B. de Rossiter Corrêa, "Low-frequency power decoupling in single-phase applications: A comprehensive overview," *IEEE Trans. Power Electron.*, vol. 32, no. 4, pp. 2892–2912, Apr. 2017.

[11] K.-H. Chao, P.-T. Cheng, and T. Shimizu, "New control methods for single phase PWM regenerative rectifier with power decoupling function," in *Proc. Int. Conf. Power Electron. Drive Syst.*, 2009, pp. 1091–1096.

[12] J. G. Pinto, V. Monteiro, H. Gonçalves, and J. L. Afonso, "Onboard reconfigurable battery charger for electric vehicles with traction-to-auxiliary mode," *IEEE Trans. Veh. Technol.*, vol. 63, no. 3, pp. 1104–1116, Mar. 2014.

[13] R. Hou and A. Emadi, "A primary full-integrated active filter auxiliary power module in electrified vehicles with single-phase onboard chargers," *IEEE Trans. Power Electron.*, vol. 32, no. 11, pp. 8393–8405, Nov. 2017.

[14] S.-B. Yin, L.-J. Diao, W.-J. Li, R.-J. He, and H.-C. Lv, "On board energy storage and control for inter-city hybrid EMU," in *Proc. 43rd Annu. Conf. IEEE Ind. Electron. Soc.*, 2017, pp. 3889–3894.

[15] D. Yuan, S. Gu, J. Liu, Y. Zhang, and C. Lv, "Design and analysis of emergency self-traction system for urban rail transit vehicles," *Energy Procedia,* vol. 16, pp. 585–591, Apr. 2012.

[16] H. Zhang, X. Li, B. Ge, and R. S. Balog, "Capacitance, dc voltage utilization, and current stress: Comparison of double-line frequency ripple power decoupling for single-phase systems," *IEEE Ind. Electron. Mag.*, vol. 11, no. 3, pp. 37–49, Sep. 2017.

[17] R. Wang *et al.*, "A high power density single-phase PWM rectifier with active ripple energy storage," *IEEE Trans. Power Electron.*, vol. 26, no. 5, pp. 1430–1443, May 2011.

[18] D. Neumayr, G. C. Knabben, E. Varescon, D. Bortis, and J. W. Kolar, "Comparative evaluation of a full- and partial-power processing active power buffer for ultracompact single-phase DC/AC converter systems," *IEEE J. Emerg. Sel. Topics Power Electron.*, vol. 9, no. 2, pp. 1994–2013, Apr. 2021.

[19] B. Ge *et al.*, "Direct instantaneous ripple power predictive control for active ripple decoupling of single-phase inverter," *IEEE Trans. Ind. Electron.*, vol. 65, no. 4, pp. 3165–3175, Apr. 2018.

[20] S. Li, W. Qi, S.-C. Tan, and S. Y. Hui, "Enhanced automatic-power-decoupling control method for single-phase AC-to-DC converters," *IEEE Trans. Power Electron.*, vol. 33, no. 2, pp. 1816–1828, Feb. 2018.

[21] M. Chen, Z. Ye, Y. Chen, and D. Xu, "Zero-voltage-switching single-phase full-bridge inverter with active power decoupling," *IEEE Trans. Power Electron.*, vol. 36, no. 1, pp. 571–582, Jan. 2021.

[22] D. Neumayr, D. Bortis, and J. W. Kolar, "Ultra-compact power pulsation buffer for single-phase DC/AC converter systems," in *Proc. IEEE 8th Int. Power Electron. Motion Control Conf*., 2016, pp. 2732–2741.

[23] N. Kumar and P. Sensarma, "Active power decoupling for differential buck inverter using virtual resistor," in *Proc. IEEE Int. Conf. Power Electron., Drives Energy Syst.*, 2020, pp. 1–6.

[24] G. Jia, M. Chen, S. Tang, C. Zhang, and G. Zhu, "Active power decoupling for a modified modular multilevel converter to decrease submodule capacitor voltage ripples and power losses," *IEEE Trans. Power Electron.*, vol. 36, no. 3, pp. 2835–2851, Mar. 2021.

[25] H. Li, K. Zhang, and H. Zhao, "DC-link active power filter for high-power single-phase PWM converters," *J. Power Electron.*, vol. 12, no. 3, pp. 458–467, May 2012.

[26] L. Bai, K. Li, Y. Wu, Q. Hui, and X. Ren, "Efficiency optimization for active storage unit with adaptive digital control," in *Proc. IEEE 3rd Int. Future Energy Electron. Conf. ECCE Asia*, 2017, pp. 1280–1285.

[27] Z. Kong, X. Huang, Z. Wang, J. Xiong, and K. Zhang, "Active power decoupling for submodules of a modular multilevel converter," *IEEE Trans. Power Electron.*, vol. 33, no. 1, pp. 125–136, Jan. 2018.

[28] H. Yuan, S. Li, W. Qi, S.-C. Tan, and S.-Y. Hui, "On nonlinear control of single-phase converters with active power decoupling function," *IEEE Trans. Power Electron.*, vol. 34, no. 6, pp. 5903–5915, Jun. 2019.

[29] H. Yuan, S. Li, S.-C. Tan, and S. Y. R. Hui, "Internal dynamics stabilization of single-phase power converters with Lyapunov-based automatic-power-decoupling control," *IEEE Trans. Power Electron.*, vol. 35, no. 2, pp. 2160–2169, Feb. 2020.

[30] Y. Man, F. Guo, and C. Bian, "The research on three-phase PWM rectifier at low switching frequency under disturbance," in *Proc. 2nd Int. Conf. Control Sci. Syst. Eng.*, 2016, pp. 159–164.

[31] H. Deng, R. Oruganti, and D. Srinivasan, "PWM methods to handle time delay in digital control of a UPS inverter," *IEEE Power Electron. Lett.*, vol. 3, no. 1, pp. 1–6, Mar. 2005.

[32] S. Li, A. T. Lee, S.-C. Tan, and S. Y. R. Hui, "Plug-and-play voltage ripple mitigator for DC links in hybrid AC–DC power grids with local bus-voltage control," *IEEE Trans. Ind. Electron.*, vol. 65, no. 1, pp. 687–698, Jan. 2018.

[33] N. Deshmukh, S. Prabhakar, and S. Anand, "Power loss reduction in buck converter based active power decoupling circuit," *IEEE Trans. Power Electron.*, vol. 36, no. 4, pp. 4316–4325, Apr. 2021.

[34] M. J. Brand, M. H. Hofmann, S. S. Schuster, P. Keil, and A. Jossen, "The influence of current ripples on the lifetime of lithium-ion batteries," *IEEE Trans. Veh. Technol.*, vol. 67, no. 11, pp. 10438–10445, Nov. 2018.

[35] L.-R. Chen, S.-L. Wu, D.-T. Shieh, and T.-R. Chen, "Sinusoidal-ripple-current charging strategy and optimal charging frequency study for Li-ion batteries," *IEEE Trans. Ind. Electron.*, vol. 60, no. 1, pp. 88–97, Jan. 2013.

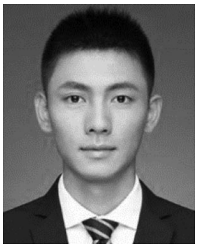

Lailai Shen was born in Anhui, China. He received the B.S. degree in electrical engineering in 2017 from Beijing Jiaotong University, Beijing, China, where he is currently working toward the Ph.D. degree in power electronics and electrical drives.

His current research interests include advanced control of dc–dc converter, motor drive, and active power decoupling.

Jie Chen (Member, IEEE) was born in Zhejiang, China. He received the B.S. degree and the Ph.D. degree in electrical engineering from Beijing Jiaotong University, Beijing, China, in 2008 and 2013, respectively.

From 2013, he was a Postdoctoral Research with Beijing Jiaotong University, Beijing, China, and the Institute of Electrical Engineering, Chinese Academy of Sciences, Beijing, China. He was a Visiting Scholar with Wisconsin Electric Machines and Power Electronics Consortium, University of Madison. He is currently an Associate Professor with Beijing Jiaotong University. His research interests include variable frequency drive, rail transportation traction control, and inverter parallel control.

Zheming Jin (Member, IEEE) was born in Jilin, China. He received the B.S. degree in electrical engineering and the M.S. degree in power electronics and ac drives from Beijing Jiaotong University, Beijing, China, in 2013 and 2015, respectively, and the Ph.D. degree in power electronic systems from the Department of Energy Technology, Aalborg University, Aalborg, Denmark, in 2018.

In 2019, he joined the Department of Energy Technology, Aalborg University, as a Postdoctoral Researcher, and was subsequently appointed as an Assistant Professor. In 2021, he joined Beijing Jiaotong University, where he is currently an Associate Professor. His research interests include control of power electronic converters, stability of power electronic-based power systems, energy storage, dc microgrids, and their applications in transportation electrification.

Zhigang Liu was born in Shandong, China, in 1961. He received the bachelor's, master's, and Ph.D. degrees in electric drive for locomotives from Beijing Jiaotong University, Beijing, China, in 1986, 1990, and 1994, respectively.

He is currently a Full Professor with Beijing Jiaotong University. In recent years, he presided over a number of national key scientific research projects and achieved fruitful results in the field of rail transit power supply, traction control, safety prediction and control, etc. He authored or coauthored a book on power electronics and spent several months as a Visiting Scholar in the U.S. and Canada. His teaching activities and research interests include power electronics circuit and system, rail transportation traction control and safety, etc.

Dr. Liu is a Vice Chairman of the China Electrotechnical Society Rail Transport Electrical Technical Committee and an Evaluation Expert of several national key plans.

Dao Zhou (Senior Member, IEEE) received the B.S. degree from Beijing Jiaotong University, Beijing, China, in 2007, the M.S. degree from Zhejiang University, Hangzhou, China, in 2010, and the Ph.D. degree from Aalborg University, Aalborg, Denmark, in 2014, all in electrical engineering.

Since 2014, he has been with the Department of Energy Technology, Aalborg University, where he is currently an Associate Professor. His research interests include modeling, control, and reliability of power electronics in renewable energy applications.

Dr. Zhou was a recipient of a few IEEE prized paper awards. He serves as an Associate Editor for the *IET Renewable Power Generation* and *IET Power Electronics*.

Chao Wu (Member, IEEE) was born in Hubei Province, China. He received the B.Eng. degree from the HeFei University of Technology, Hefei, China, and the Ph.D. degree from Zhejiang University, Hangzhou, China, in 2014 and 2019, resepctively, both in electrical engineering.

He is currently a Postdoctoral Researcher with the Department of Energy Technology, Aalborg University, Aalborg, Denmark. His current research interests focus on the cooperative control of multiconverter systems, particularly the control and operation of doubly fed induction generators for dc connection and the transient stability of power converters.